

SELF PRE-TRAINING WITH TOPOLOGY- AND SPATIALITY-AWARE MASKED AUTOENCODERS FOR 3D MEDICAL IMAGE SEGMENTATION

Pengfei Gu, Yejia Zhang, Huimin Li, Chaoli Wang, and Danny Z. Chen*

ABSTRACT

Masked Autoencoders (MAEs) have been shown to be effective in pre-training Vision Transformers (ViTs) for natural and medical image analysis problems. By reconstructing missing pixel/voxel information in visible patches, a ViT encoder can aggregate contextual information for downstream tasks. But, existing MAE pre-training methods, which were specifically developed with the ViT architecture, lack the ability to capture geometric shape and spatial information, which is critical for medical image segmentation tasks. In this paper, we propose a novel extension of known MAEs for self pre-training (i.e., models pre-trained on the same target dataset) for 3D medical image segmentation. (1) We propose a new topological loss to preserve geometric shape information by computing topological signatures of both the input and reconstructed volumes, learning geometric shape information. (2) We introduce a pre-text task that predicts the positions of the centers and eight corners of 3D crops, enabling the MAE to aggregate spatial information. (3) We extend the MAE pre-training strategy to a hybrid state-of-the-art (SOTA) medical image segmentation architecture and co-pretrain it alongside the ViT. (4) We develop a fine-tuned model for downstream segmentation tasks by complementing the pre-trained ViT encoder with our pre-trained SOTA model. Extensive experiments on five public 3D segmentation datasets show the effectiveness of our new approach.

Index Terms— Self-supervised Learning, Masked Autoencoders, Topology, Spatiality, 3D Medical Image Segmentation

1. INTRODUCTION

Accurate segmentation of medical images is critical for medical analysis and applications such as diagnosis, treatment planning, and research. While many deep learning (DL) models, such as nnU-Net [1], nnFormer [2], and UNETR++ [3], have demonstrated impressive performances in 3D medical

image segmentation, such methods still face several key challenges. A primary challenge is the scarcity of high-quality labeled medical images for model training, due to high costs and expertise needed for data collection and annotation. Another challenge is annotation errors, as labeling 3D medical images can be very time-consuming and error-prone.

Self-supervised learning (SSL), a technique that leverages pre-text tasks to derive useful visual representations from unlabeled data, offers a promising avenue to combat the challenge of label scarcity. One representative methodology for SSL is Masked Autoencoders (MAEs) [4]. Specifically, MAE learns to reconstruct the missing pixels after randomly masking a certain fraction (e.g., 75%) of patches of the input images. This approach has been successfully deployed in various applications, including in image domain [5, 6], video domain [7, 8, 9], and language domain [10, 11].

In the medical image segmentation area, MAE pre-training has also been found to be effective (e.g., UNETR + MAE [12]). Although simple and effective, there are still several limitations. First, geometric shape information (i.e., contextual information on the overall shapes of objects), which is critical for improving segmentation performance, is not captured well (e.g., see Fig. 1). Second, global spatial information is not well explored since the focus has been on reconstructing information from the masked local sub-volumes, possibly neglecting the global context information of the target objects as a whole. Third, the MAE pre-training strategy (i.e., learning representations by reconstructing missing patches from masked image input) is not exploited well with various common medical image segmentation architectures, e.g., those based on convolutional neural networks (CNNs) or hybrid models. This is primarily because MAE was developed using the Vision Transformer (ViT) [13] architecture, potentially restricting its adaptability and effectiveness with other architectures.

To address these limitations, we propose a novel extension of MAEs for self pre-training for 3D medical image segmentation. (I) We extract geometric shape information by exploiting multi-scale topological features (e.g., connected components, cycles/loops, and voids). Our method utilizes cubical complexes [14, 15] to compute topological signatures of both the input and reconstructed volumes, and employs an optimal transport distance (the 2-Wasserstein distance [16]) to derive a new topological loss. Our topology-aware loss is fully differ-

* P. Gu is with the Department of Computer Science, University of Texas Rio Grande Valley, Edinburg, TX 78539, USA. H. Li is with Department of Mathematical Sciences, The University of Texas at Dallas, Richardson, TX 75080, USA. Y. Zhang, C. Wang, and D. Chen are with the Department of Computer Science and Engineering, University of Notre Dame, Notre Dame, IN 46556, USA. E-mail: pengfei.gu01@utrgv.edu, dchen@nd.edu

entiable, computationally efficient, can be added to any neural network, and is applicable to 2D/3D images. (II) We propose a pre-text task to predict the positions of multiple key points of crops, enabling the model to aggregate spatial information. Specifically, our method predicts the positions of nine points (the center and eight corners) of a 3D crop in the input volume. By learning where the crops are located in the input volume, the model can capture global spatial information. (III) We extend the MAE pre-training strategy to a hybrid state-of-the-art (SOTA) medical image segmentation architecture, UNETR++ [3], and co-pretrain UNETR++ alongside the ViT. Specifically, masked crops are processed separately by both ViT and UNETR++ to reconstruct the associated missing patches. Reconstruction consistency loss and spatial consistency loss (derived from the pre-text task) are employed to connect the two different types of architectures in pre-training, enhancing their representation learning capability.

Following [12], our method is performed on self pre-training paradigms (i.e., models pre-trained on the same target dataset). In the self pre-training stage, we randomly mask a fraction (e.g., 50%) of patches of the image crops. The masked crops are then processed independently by a ViT model and a UNETR++ model, which are pre-trained with our proposed topological loss, pre-text task that predicts the positions of 9 key points of crops, and spatial and reconstruction consistency losses, learning the geometric shape and global spatial information and enhancing the representation learning capability. In the fine-tuning stage, the pre-trained ViT encoder is complemented with the pre-trained UNETR++ model, which is then fine-tuned for the target segmentation task. A fusion module is utilized to fuse the scale-wise features from both the pre-trained ViT encoder and UNETR++ encoder.

Our main contributions are summarized as follows:

1. We propose a new topological loss and introduce a pre-text task for MAEs to learn geometric shape and spatial information.
2. We extend the MAE pre-training strategy to a hybrid SOTA medical image segmentation architecture and co-pretrain it alongside ViT.
3. We develop a fine-tuned model for downstream segmentation tasks, and demonstrate the effectiveness of our new approach on five public 3D segmentation datasets.

2. RELATED WORK

In this section, we review recent methods pertinent to our work, including SSL, MAE, topology-based DL methods, and related DL-based medical image segmentation architectures.

Self-supervised Learning (SSL). SSL is widely recognized as an effective way to alleviate the annotation burden as it can learn useful visual representations from unlabeled data. Most known SSL methods can be categorized as either

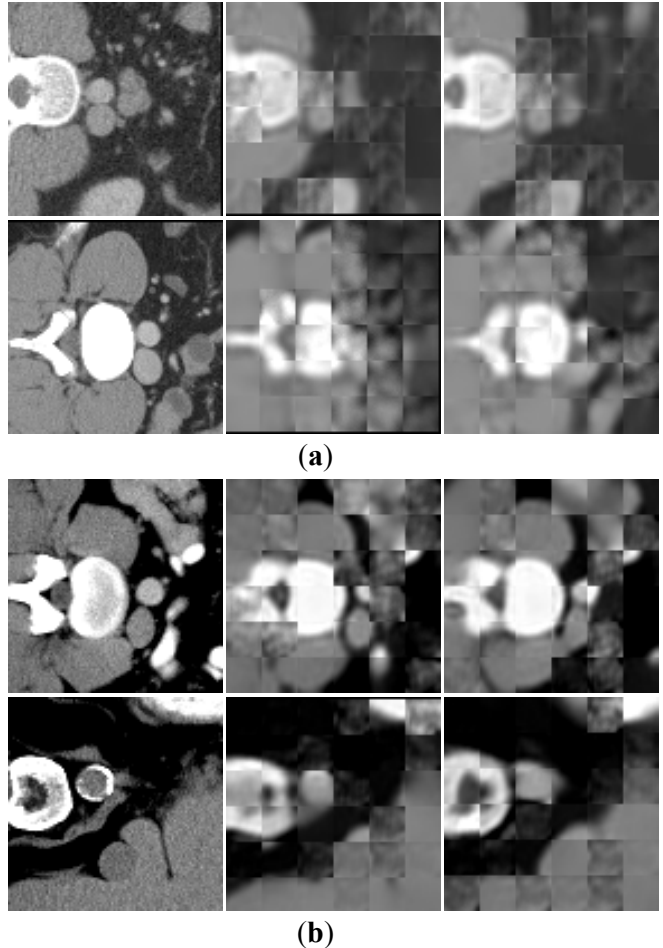


Fig. 1. Illustrating the effect of our proposed topological loss. Left column: raw image examples; middle column: reconstructed images with the mean squared error (MSE) loss [12]; right column: reconstructed images with a combination of the MSE and proposed topological losses. (a) Image examples of the Synapse multi-organ CT segmentation dataset [17]. (b) Image examples of spleen segmentation on the Medical Segmentation Decathlon (MSD) dataset [18]. The proposed topological loss helps to effectively recover objects with correct topology.

generative or discriminative.

Generative SSL methods commonly learn image representations by generating images pixel-for-pixel, using training images as supervision. The typical methods include image generation with GAN [19], super-resolution [20], image inpainting [21], image decoupling [22], and image colorization [23]. But, pixel-for-pixel generation incurs high computation costs and is difficult to learn more abstract latent representations.

Discriminative SSL methods often learn image representations by constructing discriminative pre-text tasks. Com-

mon pre-text tasks include image jigsaw puzzle [24], geometric transformations [25], and clustering [26]. Recently, contrastive learning, a new discriminative SSL method, has shown strong performance. SimCLR [27] and MoCo [28] are two typical contrastive learning methods that seek to learn representations by attracting positive pairs and repulsing negative pairs. However, these methods rely on a large number of negative samples in order to work well. BYOL [29] improved contrastive learning by directly predicting the representation output from another view and discarding negative pairs, yielding SOTA performance. SimSiam [30] further showed that stop-gradient plays an essential role in the learning stability of siamese neural networks. Since positive pairs in BYOL come from the same image, feature diversity from different images is ignored.

While our approach is SSL, it targets self pre-training paradigms for 3D medical image segmentation.

Masked Autoencoders (MAEs). MAEs [4] are a type of denoising autoencoders [31] that learn representations by reconstructing the original input from masked input. The introduction of masked language modeling in BERT [32] gave a transformative impact on natural language processing (NLP). Recently, several studies applied MAEs to medical image analysis [33, 6, 12, 34, 35, 36]. In [12], it showed that directly applying MAEs to medical datasets yields superior performance over its counterpart pre-trained on ImageNet [37]. In [6], it exhibited that MAEs can help 3D medical image analysis, besides natural images. In [34, 35], it proved that adding an additional global loss on top of a local loss can make representations more semantically meaningful. In [33], it directly applied MAEs to medical image classification. A self-distillation loss was used to improve MAE pre-training [36].

Different from these known methods, our approach emphasizes extending the MAE pre-training strategy to a hybrid medical image segmentation architecture, enhancing its ability to learn geometric shape and global spatial information.

Topology-based Deep Learning Methods. Topology is often referred to as encoding the overall shapes of data. Numerous works aim to leverage topological information in DL methods to tackle various biomedical image analysis tasks.

For segmentation tasks, pre-trained filters were leveraged to detect higher-order topological features of linear structures [38]. cDice [39] proposed an additional Dice loss for extracted skeleton structures, guaranteeing topology preservation. A persistent homology (PH) based loss was designed for DL architectures [40, 41], learning to segment with correct topology. DMT-loss [42] utilized discrete Morse theory to identify topologically critical structures for segmentation.

For classification tasks, a new topological regularizer was proposed [43] to train classifiers for classifying kidney and brain cell cancers. A unified model was presented that aggregates appearance, microenvironment, and topology for pathology image classification [44]. For reconstruction tasks,

a multi-scale topological loss was proposed [45] to capture shape information for 3D reconstruction (i.e., reconstructing 3D objects from 2D images).

For other tasks, a method was introduced to detect topological handles for cardiac trabeculae restoration [46]. A topology-aware generative adversarial network was proposed to generate images with correct topology [47]. Topographical features were computed for clustering high dimensional categorical data [48]. A GO-term embedding based method was proposed for protein semantic similarity prediction [49].

Different from these known methods, our method computes a new topological loss on raw images. To our best knowledge, no known methods employ a topology-aware loss for self pre-training for 3D medical image segmentation.

DL Medical Image Segmentation Methods. Most DL medical image segmentation methods can be categorized as CNN-based, Transformer-based, or hybrid. Many CNN-based segmentation methods are extended from the standard U-Net architecture [50]; some typical such models include Attention U-Net [51], UNet++ [52], UNet 3+ [53], and nnU-Net [1].

Due to their ability to encode long-range dependencies, ViTs recently gained popularity. A main building block in the Transformer architecture is the self attention operation that models interactions among a sequence of image patches, thus learning global relationships. There are a few pure Transformer-based methods for medical image segmentation [54, 55].

The known hybrid methods combine convolutions and self-attention operations for better segmentation. Recent common hybrid methods include TransUNet [56], UNETR [57], MISSFormer [58], Swin UNETR [59], nnFormer [2], UNETR++ [3], TransBTS [60], CoTr [61], TransFuse [62], MedT [63], and ConvFormer [64].

In this work, our focus is not on proposing a new DL architecture for 3D medical image segmentation. Instead, we aim to construct a fine-tuned model on top of an existing SOTA architecture (i.e., UNETR++ [3]).

3. METHOD

Fig. 2 presents an overview of our proposed pipeline, which contains four main components: (1) a topological loss that aims at implicitly extracting geometric shape information by exploiting multi-scale topological features; (2) a pre-text task that captures global spatial information by predicting the positions of 9 key points of 3D crops in the input volume; (3) a spatial consistency loss and a reconstruction consistency loss that enhance the representation learning capability of both the ViT and UNETR++ models by aligning the reconstructed images at both spatial and image levels; (4) a fine-tuned model for improving the downstream segmentation performance.

In Subsection 3.1, we introduce the topological loss for extracting the topology of the input volume. In Subsec-

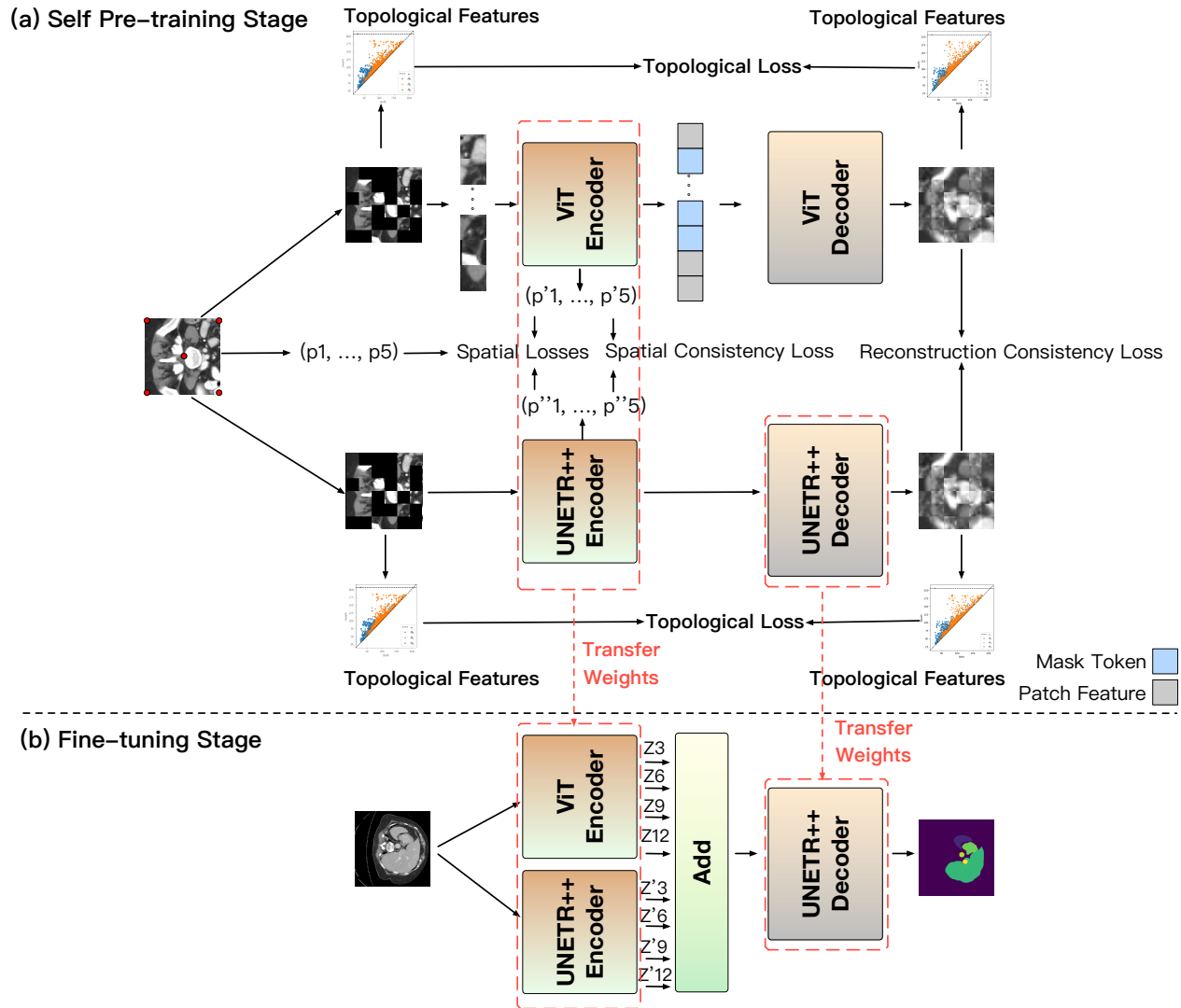


Fig. 2. An overview of our proposed pipeline. In the self pre-training stage, we randomly mask a fraction (e.g., 50%) of patches of the 3D crops. The masked crops are processed independently by both a ViT model and a UNETR++ model [3], which are pre-trained with our proposed topological loss, pre-text task that predicts the positions of 9 key points of the crops, and spatial and reconstruction consistency losses for learning geometric shape and global spatial information. In the fine-tuning stage, the pre-trained ViT encoder is complemented with the pre-trained UNETR++ model, which is then fine-tuned for the target segmentation task. For visual simplicity, this illustration uses images instead of sub-volumes (displayed in 2D), shows only 5 key points (the five red points in the original image in (a)) for the spatial loss, and omits the MSE reconstruction loss for the two branches in the self pre-training stage in (b).

tion 3.2, we propose the pre-text task for capturing global spatial information. In Subsection 3.3, we present the spatial and reconstruction consistency losses for co-pretraining the ViT and UNETR++ models. In Subsection 3.4, we construct the fine-tuned architecture for the downstream segmentation tasks.

3.1. Capturing the Topology of Input Volumes

Given a 3D image I , we represent I with a *cubical complex* C . Typically, the cubical complex C takes each voxel of I as an individual vertex and contains connectivity information on vertex neighbourhoods via edges, squares, and their higher-dimensional counterparts [14, 15]. In this work, we use *persistent homology* (PH) [65] to extract topological features of different dimensions from C , including connected components (0-D), cycles/loops (1-D), and voids (2-D). PH com-

bins the homology of super-level sets by sweeping a threshold function through the entire real numbers. Specifically, for a threshold value $\tau \in \mathbb{R}$, a cubical complex is defined as:

$$C^{(\tau)} := \{x \in I \mid f(x) \geq \tau\}, \quad (1)$$

where $f(x)$ is the voxel value of x . When sweeping the threshold, the topology changes only at a finite number of values, $\tau_1 \geq \tau_2 \geq \dots \geq \tau_{m-1} \geq \tau_m$, and we obtain a sequence of nested cubical complexes, $\emptyset \subseteq C^{(\tau_1)} \subseteq C^{(\tau_2)} \subseteq \dots \subseteq C^{(\tau_{m-1})} \subseteq C^{(\tau_m)} = I$, which forms the *super-level set filtration*. PH tracks topological features across all the complexes in this filtration, representing each feature as a tuple (τ_i, τ_j) with $\tau_i \geq \tau_j$, indicating the cubical complex in which a feature appears and disappears, respectively. For example, a 0-D tuple (τ_i, τ_j) represents a connected component that appears at threshold τ_i and disappears at threshold τ_j . The tuples of the k -D ($0 \leq k \leq 2$) features are saved in the k -th *persistence diagram* D_I^k , which is a multi-scale shape descriptor of all topological features of the 3D image I .

Comparing Persistence Diagrams. Given two persistence diagrams D and D' , we use the *2-Wasserstein distance* [16] as a metric to measure their similarity or distance, defined as:

$$W_2(D, D') := \left(\inf_{\eta: D \rightarrow D'} \sum_{x \in D} \|x - \eta(x)\|_\infty^2 \right)^{\frac{1}{2}}, \quad (2)$$

where $\eta(\cdot)$ denotes a bijection. Note that Eq. (2) can be solved by using an optimal transport algorithm [66], and we use cubical Ripser [15] to compute PHs from volumes.

Constructing Topological Loss. Given an input volume I and a reconstructed volume I' , our new topology-aware loss is defined as:

$$\mathcal{L}_{topo}(I, I') = \left(\sum_{i=0}^2 (W_2(D_I^i, D_{I'}^i))^2 \right)^{\frac{1}{2}}, \quad (3)$$

where $W_2(\cdot, \cdot)$ denotes the 2-Wasserstein distance, and D_I^i and $D_{I'}^i$ are the i -D persistence diagrams of I and I' , respectively. Note that our proposed topological loss differs from that in [45]. First, we extract topological features from 3D images, not from the segmentation. Second, we use the topological loss for self pre-training and medical image segmentation, not for 3D reconstruction tasks.

3.2. Exploiting Global Spatial Information

MAE [4] and UNETR + MAE [12] lack the ability to learn global spatial information that is vital to 3D medical image segmentation for two reasons: (1) The positional embedding encodes only local position information for each patch, and (2) the methods focus only on low-level patch matching with a local mean squared error (MSE) loss. To address these limitations, we propose a novel pre-text task that complements

the known methods with global spatial information. Specifically, the pre-text task aims to predict the positions of 9 key points (the center and eight corners) of 3D crops in the input volume. We attain this by adding two prediction heads to the ViT and UNETR++ encoders. The two prediction heads share the same architecture that consists of a convolutional layer, a two-layer multilayer perceptron (MLP) with 256 hidden dimensions, and a tanh activation function. This design enables the ViT and UNETR++ encoders to learn global spatial representations.

Constructing Spatial Loss. We denote the 9 key points of a 3D crop as (p_1, p_2, \dots, p_9) , where p_9 is for the crop center, and each $p_i = (x_i, y_i, z_i)$. Given the ground truth (GT) and the prediction of the 9 positions, $P = (p_1, p_2, \dots, p_9)$ and $P' = (p'_1, p'_2, \dots, p'_9)$, the spatial loss is defined as:

$$\mathcal{L}_{spa}(P, P') = \mathcal{L}_{MSE}(P, P'), \quad (4)$$

where \mathcal{L}_{MSE} is the MSE loss. Note that our spatial loss definition and implementation are different from those in [67].

3.3. Co-pretraining the ViT and UNETR++ Models

As illustrated in Fig. 2, the masked crops are processed independently by both the ViT and UNETR++ models. To co-pretrain both the ViT and UNETR++ models to enhance their representation learning capability, we propose to align the reconstructed images in the spatial and image levels.

Constructing Spatial Consistency Loss. Given predictions of 9 key point positions from the ViT and UNETR++ encoders, $P' = (p'_1, p'_2, \dots, p'_9)$ and $P'' = (p''_1, p''_2, \dots, p''_9)$, the spatial consistency loss is defined as:

$$\mathcal{L}_{spa-consis}(P', P'') = \mathcal{L}_{MSE}(P', P''). \quad (5)$$

The spatial consistency loss aligns the reconstructed images at the spatial level, enhancing the representation learning capability of both the ViT and UNETR++ models.

Constructing Reconstruction Consistency Loss. Given reconstructed volumes I' and I'' by the ViT and UNETR++ models, our reconstruction consistency loss function computes the MSE between the reconstructed volumes I' and I'' , as:

$$\mathcal{L}_{rec-consis}(I', I'') = \mathcal{L}_{MSE}(I', I''). \quad (6)$$

We compute this loss only on masked patches, similar to MAE in [4]. The reconstruction consistency loss aligns the reconstructed images at the image level, further enhancing the representation learning capability of both ViT and UNETR++.

The Overall Loss of Self Pre-training. The overall loss for a volume crop is:

$$\begin{aligned} \mathcal{L} = & (1 - \lambda_1)(1 - 2\lambda_2)\mathcal{L}_{MSE-ViT} + (1 - \lambda_1)\lambda_2\mathcal{L}_{topo-ViT} \\ & + (1 - \lambda_1)\lambda_2\mathcal{L}_{spa-ViT} + \lambda_1(1 - 2\lambda_2)\mathcal{L}_{MSE-UNETR++} \\ & + \lambda_1\lambda_2\mathcal{L}_{topo-UNETR++} + \lambda_1\lambda_2\mathcal{L}_{spa-UNETR++} \\ & + \lambda_3\mathcal{L}_{spa-consis} + \lambda_3\mathcal{L}_{rec-consis}, \end{aligned}$$

where \mathcal{L}_{MSE-X} , \mathcal{L}_{topo-X} , and \mathcal{L}_{spa-X} are the reconstruction, topological, and spatial losses, respectively, for the X (either ViT or UNETR++) model, and λ_i is a balancing weight.

3.4. Constructing the Fine-tuned Architecture

In [12], the pre-trained ViT encoder weights were transferred to initialize the segmentation encoder, i.e., the UNETR [57] encoder, achieving impressive performance. Following [12], we utilize the pre-trained ViT encoder weights and propose to complement the pre-trained ViT encoder with the pre-trained UNETR++ [3] to enhance the performance of downstream segmentation tasks.

As shown in Fig. 2, our fine-tuned model consists of four key components: two pre-trained encoders (the pre-trained ViT and UNETR++ encoders), an add fusion module, and a pre-trained UNETR++ decoder. Specifically, the two encoders are employed to capture complementary features, since the ViT encoder is a Transformer-based architecture and the UNETR++ encoder is a convolution-based architecture. Then a scale-wise fusion module, which is addition, is used to fuse the scale-wise features from the two different types of encoders. Finally, a pre-trained UNETR++ decoder is appended to generate the final segmentation. Our fine-tuned model is called **MAE + UNETR++**, which can effectively leverage the pre-trained ViT encoder to capture high-level semantic information and the pre-trained UNETR++ to better capture fine details and edges, resulting in improved segmentation performance.

4. EXPERIMENTS AND ANALYSIS

We conduct comprehensive experiments to validate the effectiveness of our proposed approach. In Subsection 4.1, we discuss the datasets and experimental setup. In Subsection 4.2, we describe the implementation details. In Subsection 4.3, we present the metrics for evaluating the performance of our method. In Subsection 4.4, we report the experimental results. In Subsection 4.5, we show the ablation study to examine the effects of different key components in our method.

4.1. Datasets and Experimental Setup

We conduct experiments on five segmentation datasets: Synapse multi-organ CT segmentation [17], BTCV multi-organ CT segmentation [17], ACDC automated cardiac diagnosis [68], and Medical Segmentation Decathlon (MSD) datasets [18] for two different segmentation tasks, spleen segmentation and lung segmentation. For each experiment, we perform 5 runs using different random seeds and report the average results. Additionally, we compute p -values to ascertain the statistical significance of the results.

The Synapse Multi-organ CT Segmentation Dataset (Synapse CT Dataset)¹: This dataset [17] contains 30 abdominal CT volumes with 8 organs. Following [56], we split the dataset randomly into 18 volumes and 12 volumes for training and testing, and report the average Dice and 95% Hausdorff distance (HD95) on 8 abdominal organs: spleen (Spl), right kidney (RKid), left kidney (LKid), gallbladder (Gal), liver (Liv), stomach (Sto), aorta (Aor), and pancreas (Pan).

The BTCV Multi-organ CT Segmentation Dataset (BTCV CT Dataset)¹: This dataset [17] consists of 30 abdominal CT volumes with 13 organs, including 8 organs of the Synapse CT dataset, along with esophagus (Eso), inferior vena cava (IVC), portal and splenic veins (PSV), right adrenal gland (RAG), and left adrenal gland (LAG). We report the average Dice scores on all the 13 abdominal organs, following [3].

ACDC Automated Cardiac Diagnosis (ACDC Dataset)²: This dataset [68] contains 100 samples, and aims to segment the cavity of the right ventricle, the myocardium of the left ventricle, and the cavity of the left ventricle. Each sample’s labels involve left ventricle (LV), right ventricle (RV), and myocardium (MYO). Following [2], we split the dataset into 70 training samples, 10 validation samples, and 20 test samples, and use the Dice score as the evaluation metric.

Spleen Segmentation on the MSD Dataset (MSD Spleen Dataset)³: This dataset [18] contains 41 CT volumes for spleen segmentation. Following [57], we split the dataset into training, validation, and test sets with a ratio of 80:15:5, and use the Dice score and HD95 as the evaluation metrics.

Lung Segmentation on the MSD Dataset (MSD Lung Dataset)³: This dataset [18] comprises 64 CT volumes, aiming to segment lung cancer from the background. We split the dataset with a 80:20 ratio for training and testing, and use the Dice score as the evaluation metric, as in [3].

4.2. Implementation Details

Our experiments are implemented with PyTorch and MONAI.⁴ The model training is performed on an NVIDIA Tesla V100 Graphics Card with 32GB GPU memory using the AdamW optimizer [69] with a weight decay = 0.005.

For the Synapse CT and BTCV CT datasets, we clip the raw values between -175 and 250 , normalize the values into the range of $[0, 1]$, and re-sample the spacing to $[1.5, 1.5, 2.0]$. All the models are trained with input images of size $96 \times 96 \times 96$. For the ACDC dataset, we re-sample the spacing to $[1.52, 1.52, 6.35]$. All the models are trained with input of size $160 \times 160 \times 16$. For the MSD spleen dataset, we clip the

¹<https://www.synapse.org/#!/Synapse:syn3193805/wiki/89480>

²<https://www.creatis.insa-lyon.fr/Challenge/acdc/databases.html>

³<http://medicaldecathlon.com/dataaws/>

⁴<https://github.com/Project-MONAI>

Table 1. Segmentation results of different methods on the Synapse CT dataset. The results of the baselines are from [3, 12]. “—” indicates that the results were not reported in the original papers. The reported values are the averages of 5 runs with different random seeds. The best results are marked in **bold**, and the second-best results are underlined. We calculate the p -values between the average performance of our method and the best performing baseline in both the metrics.

Method	Params.	FLOPs	Spl	RKid	LKid	Gal	Liv	Sto	Aor	Pan	Average	
											Dice (\uparrow)	HD95 (\downarrow)
U-Net [50]	—	—	86.67	68.60	77.77	69.72	93.43	75.58	89.07	53.98	76.85	—
TransUNet [56]	96.07M	88.91	85.08	77.02	81.87	63.16	94.08	75.62	87.23	55.86	77.49	31.69
UNETR [57]	92.49M	75.76	85.00	84.52	85.60	56.30	94.57	70.46	89.80	60.47	78.35	18.59
Swin-UNet [55]	—	—	90.66	79.61	83.28	66.53	94.29	76.60	85.47	56.58	79.13	21.55
MISSFormer [58]	—	—	91.92	82.00	85.21	68.65	94.41	80.81	86.99	65.67	81.96	18.20
Swin UNETR [59]	62.83M	384.2	95.37	86.26	86.99	66.54	95.72	77.01	91.12	68.80	83.48	10.55
UNETR + MAE [12]	—	—	90.56	84.00	86.37	<u>75.25</u>	95.95	80.89	88.92	65.02	83.52	10.24
nnFormer [2]	150.5M	213.4	90.51	86.25	86.57	70.17	<u>96.84</u>	<u>86.83</u>	92.04	83.35	86.57	10.63
UNETR++ [3]	42.96M	47.98	95.77	<u>87.18</u>	<u>87.54</u>	71.25	96.42	86.01	<u>92.52</u>	81.10	<u>87.22</u>	<u>7.53</u>
MAE + UNETR++ (ours)	85.96M	82.49	<u>95.68</u>	89.30	87.64	79.60	96.98	88.47	92.58	<u>81.27</u>	88.94 (1.72% \uparrow)	5.89 (1.64 \uparrow)
p -values	$< 5e - 2$ (Dice), $< 1e - 2$ (HD95)											

raw values between -57 and 164 , normalize the values into the range of $[0, 1]$, and re-sample the spacing to $[1.5, 1.5, 2.0]$. All the models are trained with input of size $96 \times 96 \times 96$. For the MSD lung dataset, we clip the raw values between -1000 and 3071 , normalize the values into the range of $[0, 1]$, and re-sample the spacing to $[1.0, 1.0, 1.0]$. All the models are trained with input of size $192 \times 192 \times 32$.

We use a learning rate of $6.4e - 3$ for self pre-training on all the datasets. We pre-train on the Synapse CT, BTCV CT, and MSD spleen and lung segmentation datasets with 10,000 epochs, and on the ACDC dataset with 2,000 epochs.

For all the downstream segmentation tasks, we use a learning rate of $1e - 1$, and fine-tune with 5,000 epochs for the Synapse CT, BTCV CT, and MSD spleen and lung segmentation datasets, and 1,000 epochs for the ACDC dataset. The batch size for each case is set as the maximum size allowed by the GPU. We set $\lambda_1 = 0.5$, $\lambda_2 = 0.1$, and $\lambda_3 = 0.1$.

4.3. Evaluation Metrics

We use the Dice score and HD95 as the evaluation metrics to measure the performances of the methods. For a specific semantic class, let GT_i and P_i denote the GT and prediction values for a voxel i , and GT and P denote the GT and prediction point sets, respectively.

The Dice score is defined as:

$$\text{Dice}(GT, P) = \frac{2 \sum_i GT_i \times P_i}{\sum_i GT_i + \sum_i P_i}. \quad (7)$$

The Hausdorff distance (HD) is defined as:

$$\text{HD}(GT, P) = \max\{\max_{g \in GT} \min_{p \in P} \|g - p\|, \max_{p \in P} \min_{g \in GT} \|p - g\|\}. \quad (8)$$

The HD95 uses the 95th percentile of the distances between the GT and prediction point sets.

4.4. Experimental Results

Synapse CT Dataset Results. In Table 1, we compare our method with an array of baseline methods (U-Net [50], TransUNet [56], UNETR [57], Swin-UNet [55], MISSFormer [58], Swin UNETR [59], and nnFormer [2]) and SOTA models (UNETR++ [3], and the MAE-based self pre-training method, i.e., UNETR + MAE [12]). On this dataset, UNETR++ yields superior performance over the other known methods. Our method outperforms UNETR++ by 1.72% and 1.64 mm in average Dice and HD95, respectively, which are quite impressive improvements on the Synapse CT dataset. Specifically, our method achieves the highest Dice scores on six organs (kidney (right), kidney (left), gallbladder, liver, stomach, and aorta). Compared to the known methods, our method is more advantageous in segmenting gallbladder, which is difficult to delineate using known segmentation methods. Moreover, our method is able to surpass the MAE-based self pre-training method, UNETR + MAE, by large margins in both the evaluation metrics, demonstrating the effectiveness of our method.

BTCV CT Dataset Results. Table 2 showcases the segmentation results of various methods on the BTCV CT dataset. Among the known methods, nnU-Net [1] and UNETR++ [3] achieve average Dice scores of 83.16% and 83.28%, respectively. Our method outperforms the SOTA method UNETR++ by 0.8% in average Dice. This is particularly commendable given the challenging nature of the BTCV CT dataset, which encompasses 13 distinct organs.

ACDC Dataset Results. Table 3 reports the quantitative results on the ACDC dataset. We observe that nnFormer [2] and UNETR++ [3] attain better performances of 92.06% and 92.83% in average Dice, respectively. Remarkably, our method surpasses the SOTA method UNETR++ by 0.62% in the average Dice score. Furthermore, our method outperforms the MAE-based self pre-training method UNETR + MAE [12] by an impressive 3.15% in average Dice, confirming the effectiveness of our new approach.

Table 2. Segmentation results of different methods on the BTCV CT dataset. The results of the baselines are from [3]. The reported values are the averages of 5 runs with different random seeds. The best results are marked in **bold**, and the second-best results are underlined. We calculate the p -values between the average performance of our method and the best performing baseline in the average Dice score metric.

Method	Spl	RKid	LKid	Gal	Eso	Liv	Sto	Aor	IVC	PSV	Pan	RVG	LAG	Average Dice (\uparrow)
UNETR [57]	90.48	82.51	86.05	58.23	71.21	94.64	72.06	86.57	76.51	70.37	66.06	66.25	63.04	76.00
Swin UNETR [59]	94.59	88.97	92.39	65.37	75.43	95.61	75.57	88.28	81.61	76.30	74.52	68.23	66.02	80.44
TransBTS [60]	94.55	<u>89.20</u>	90.97	68.38	75.61	96.44	83.52	88.55	82.48	74.21	76.02	67.23	67.03	81.31
nnFormer [2]	94.58	88.62	93.68	65.29	76.22	96.17	83.59	89.09	80.80	75.97	77.87	70.20	66.05	81.62
nnU-Net [1]	95.95	88.35	93.02	70.13	76.72	96.51	<u>86.79</u>	88.93	82.89	78.51	<u>79.60</u>	73.26	<u>68.35</u>	83.16
UNETR++ [3]	94.94	91.90	<u>93.62</u>	<u>70.75</u>	<u>77.18</u>	<u>95.95</u>	85.15	<u>89.28</u>	<u>83.14</u>	76.91	77.42	<u>72.56</u>	68.17	<u>83.28</u>
MAE + UNETR++ (ours)	<u>94.97</u>	87.93	87.37	78.46	78.97	96.99	88.31	92.51	89.01	<u>76.94</u>	80.18	69.88	71.48	84.08 (0.8% \uparrow)
p -value	$< 1e - 2$ (Dice)													

Table 3. Segmentation results of different methods on the ACDC dataset. The results of the baselines are from [3, 2]. ‘—’ indicates that the results were not reported in the original papers, and (\cdot) specifies the results of our implementation of the known method. The reported values are the averages of 5 runs with different random seeds. The best results are marked in **bold**, and the second-best results are underlined. We calculate the p -values between the average performance of our method and the best performing baseline in the Dice score metric.

Method	RV	Myo	LV	Average
VIT-CUP [13]	81.46	70.71	92.18	81.45
R50-VIT-CUP [13]	86.07	81.88	94.75	87.57
MISSFormer [58]	86.36	85.75	91.59	87.90
UNETR [57]	85.29	86.52	94.02	88.61
TransUNet [56]	88.86	84.54	95.73	89.71
Swin-UNet [55]	88.55	85.62	95.83	90.00
LeViT-UNet-384s [70]	89.55	87.64	93.76	90.32
UNETR + MAE [12]	— (88.44)	— (87.87)	— (94.58)	— (90.30)
nnFormer [2]	90.94	89.58	95.65	92.06
UNETR++ [3]	<u>91.89</u>	<u>90.61</u>	<u>96.00</u>	<u>92.83</u>
MAE + UNETR++ (ours)	92.59	91.38	96.37	93.45 (0.62% \uparrow)
p -value	$< 1e - 2$ (Dice)			

Table 4. Segmentation results of different methods on the MSD spleen dataset. The results of the baselines are from [57]. ‘—’ indicates that the results were not reported in the original papers, and (\cdot) specifies the results of our implementation of the known method. The reported values are the averages of 5 runs with different random seeds. The best results are marked in **bold**, and the second-best results are underlined. We calculate the p -values between the average performance of our method and the best performing baseline in both the metrics.

Method	Dice (\uparrow)	HD95 (\downarrow)
SETR MLA [71]	0.950	4.091
TransUNet [56]	0.950	4.031
AttUNet [51]	0.951	4.091
U-Net [50]	0.953	4.087
CoTr [61]	0.954	3.860
UNETR [57]	0.964	1.333
UNETR + MAE [12]	— (0.966)	— (1.295)
UNETR++ [3]	<u>0.966</u>	1.246
MAE + UNETR++ (ours)	0.974 (0.8% \uparrow)	1.002 (0.244 \uparrow)
p -values	$< 1e - 2$ (Dice), $< 5e - 2$ (HD95)	

Table 5. Segmentation results of different methods on the MSD lung dataset. The results of the baselines are from [3]. ‘—’ indicates that the results were not reported in the original papers, and (\cdot) specifies the results of our implementation of the known method. The reported values are the averages of 5 runs with different random seeds. The best results are marked in **bold**, and the second-best results are underlined. We calculate the p -values between the average performance of our method and the best performing baseline in both the metrics.

Method	Dice (\uparrow)
UNETR [57]	73.29
nnU-Net [1]	74.31
Swin UNETR [59]	75.55
nnFormer [2]	77.95
UNETR + MAE [12]	— (78.90)
UNETR++ [3]	<u>80.68</u>
MAE + UNETR++ (ours)	82.55 (1.87% \uparrow)
p -value	$< 5e - 2$ (Dice)

MSD Spleen Dataset Results. As Table 4 shows, on the MSD spleen dataset, both UNETR + MAE [12] and UNETR++[3] already achieve a very high 0.966 Dice score, giving a limited margin for big improvement. Nonetheless, our method still manages to enhance both the Dice and HD95 scores by 0.8% and 0.244, respectively. These performances reinforce the superiority of our method over known SOTA methods.

MSD Lung Dataset Results. Table 5 presents the experimental results on the MSD lung dataset. One can see that the best known method is UNETR++ [3], whose Dice score is higher than the second-best method, UNETR + MAE [12], by a margin of 1.78%. In comparison, our method outperforms UNETR++ by 1.87% and UNETR + MAE by a notable 3.65% in Dice score. These substantial improvements validate the effectiveness of our method.

Statistical Significance. In Tables 1, 2, 3, 4, and 5, we employ the independent two-sample t -test to calculate the p -values between the average performance of our method and

Table 6. Ablation study of the effects of different key components in our MAE + UNETR++ approach on the Synapse CT dataset. The reported values are the averages of 5 runs with different random seeds.

Method	Pre-trained ViT Encoder	Spatial Pre-text Task	Topological Loss	Pre-trained UNETR++	Dice (\uparrow)	HD95 (\downarrow)
UNETR++					87.22	7.53
UNETR++ with pre-trained ViT encoder	✓				87.62	7.03
UNETR++ with pre-trained ViT encoder & spatial pre-text task	✓	✓			88.09	6.12
UNETR++ with pre-trained ViT encoder & spatial pre-text task & topological loss	✓	✓	✓		88.34	5.96
MAE + UNETR++	✓	✓	✓	✓	88.94	5.89

the best-performing baseline in the evaluation metrics. The null hypothesis is that our method offers no superior benefits over the best-performing baseline. As one can see from these five tables, on all the five public datasets, our method consistently delivers p -values below $5e - 2$, whether measured by HD95 and Dice or solely by Dice. This provides compelling evidence against the null hypothesis. Hence, our method yields significant improvements over known SOTA baseline methods on the five public datasets.

4.5. Ablation Study

We conduct ablation study using the Synapse CT dataset to examine the effects of different key components in our method. From the results in Table 6, we observe the following. (1) When applying the pre-trained ViT encoder on top of UNETR++, the Dice is improved by 0.4% (p -value = 0.027, t -test), showing the effect of our fine-tuned model. (2) When adding the spatial pre-text task to the pre-training of ViT only, the Dice is further improved by 0.47% (p -value = 0.009, t -test), demonstrating the effect of our proposed pre-text task in extracting spatial information. (3) When further adding the topological loss to the pre-training of ViT only, the Dice is further improved by 0.25% (p -value = 0.015, t -test), validating the effect of our proposed topological loss in capturing geometric shape information. (4) When transferring the weights of both the ViT encoder and UNETR++ to the fine-tuned model, the Dice is improved by 0.60% (p -value = 0.011, t -test), validating the effects of the MAE pre-training strategy on UNETR++ as well as the spatial and reconstruction consistency losses on co-pretraining ViT and UNETR++.

4.6. Visualization of Segmentation Results

Fig. 3 displays some qualitative results by our method, UNETR++, UNETR + MAE, and UNETR on the Synapse CT dataset. Compared to the prediction results produced by the other methods, our prediction results are much closer to the ground truth (GT), showing clear advantages. Specifically, our method substantially reduces false positive predictions.

This demonstrates the capability of our method in capturing geometric shape information and extracting spatial information.

Fig. 4 provides a qualitative comparison of segmentation results by UNETR++, nnFormer, UNETR + MAE, UNETR, and our method on the ACDC dataset. In the first row, one can see that the baseline methods, UNETR++, nnFormer, UNETR + MAE, and UNETR, generate some false positive predictions. However, our method does not. This validates that our method is able to capture geometric (i.e., topological) information with the proposed topological loss. In the second row, we observe that (1) UNETR and UNETR + MAE fail to segment the complete shape of the myocardium, (2) nnFormer produces some incorrect right ventricle pixels inside the myocardium, and (3) UNETR++ misses segmenting some myocardium pixels along the boundary. In contrast, our method generates highly accurate predictions, further showing its effectiveness.

5. CONCLUSIONS

In this paper, we proposed a novel extension of masked autoencoders (MAEs) for self pre-training (i.e., models pre-trained on the same target dataset) for 3D medical image segmentation. In particular, we proposed a new topological loss for extracting geometric shape information, introduced a pre-text task to aggregate global spatial information, extended the MAE pre-training strategy to a hybrid SOTA medical image segmentation architecture, and developed a fine-tuned model to further improve the downstream segmentation performance. Experimental results on five public 3D segmentation datasets demonstrated the effectiveness of our proposed approach.

6. REFERENCES

- [1] F. Isensee, P. F. Jaeger, S. A. Kohl, J. Petersen, and K. H. Maier-Hein, "nnU-Net: A self-configuring method for deep learning-based biomedical image segmentation," *Nature Methods*, vol. 18, no. 2, pp. 203–211, 2021.

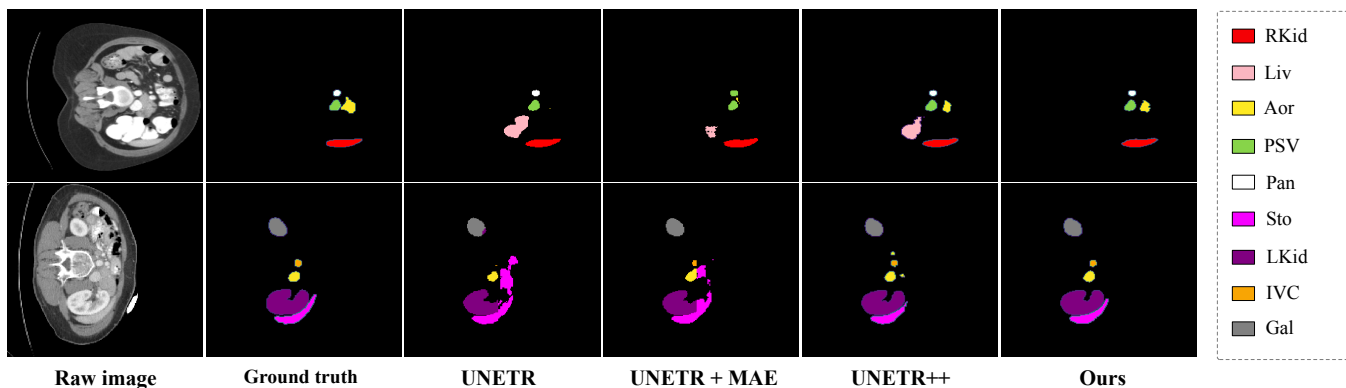


Fig. 3. Visual comparison of some qualitative segmentation results by our proposed method, UNETR++, UNETR + MAE, and UNETR on the Synapse CT dataset. The results of our method show its efficacy in more accurate segmentation. RKid: right kidney; Liv: liver; Aor: aorta; PSV: portal and splenic veins; Pan: pancreas; Sto: stomach; LKid: left kidney; IVC: inferior vena cava; Gal: gallbladder.

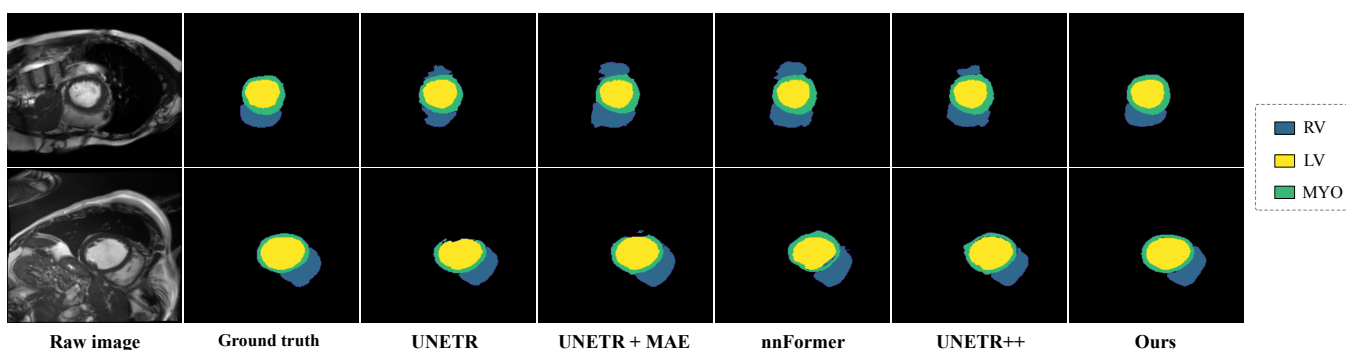


Fig. 4. Visual comparison of some qualitative segmentation results by our proposed method, UNETR++, nnFormer, UNETR + MAE, and UNETR on the ACDC dataset. The results highlight the high accuracy of our method. RV: right ventricle; LV: left ventricle; MYO: myocardium.

- [2] H.-Y. Zhou, J. Guo, Y. Zhang, L. Yu, L. Wang, and Y. Yu, “nnFormer: Interleaved Transformer for volumetric segmentation,” *arXiv preprint arXiv:2109.03201*, 2021.
- [3] A. Shaker, M. Maaz, H. Rasheed, S. Khan, M.-H. Yang, and F. S. Khan, “UNETR++: Delving into efficient and accurate 3D medical image segmentation,” *arXiv preprint arXiv:2212.04497*, 2022.
- [4] K. He, X. Chen, S. Xie, Y. Li, P. Dollár, and R. Girshick, “Masked autoencoders are scalable vision learners,” in *CVPR*, 2022, pp. 16000–16009.
- [5] Z. Xie, Z. Zhang, Y. Cao, Y. Lin, J. Bao, Z. Yao, Q. Dai, and H. Hu, “SimMIM: A simple framework for masked image modeling,” in *CVPR*, 2022, pp. 9653–9663.
- [6] Z. Chen, D. Agarwal, K. Aggarwal, W. Safta, M. M. Balan, and K. Brown, “Masked image modeling advances 3D medical image analysis,” in *WACV*, 2023, pp. 1970–1980.
- [7] C. Feichtenhofer, Y. Li, K. He, et al., “Masked autoencoders as spatiotemporal learners,” in *NeurIPS*, 2022, pp. 35946–35958.
- [8] Z. Tong, Y. Song, J. Wang, and L. Wang, “VideoMAE: Masked autoencoders are data-efficient learners for self-supervised video pre-training,” in *NeurIPS*, 2022, pp. 10078–10093.
- [9] A. Gupta, J. Wu, J. Deng, and L. Fei-Fei, “Siamese masked autoencoders,” *arXiv preprint arXiv:2305.14344*, 2023.
- [10] H. Bao, W. Wang, L. Dong, Q. Liu, O. K. Mohammed, K. Aggarwal, S. Som, S. Piao, and F. Wei, “VLMO: Unified vision-language pre-training with mixture-of-modality-experts,” in *NeurIPS*, 2022, pp. 32897–32912.
- [11] X. Geng, H. Liu, L. Lee, D. Schuurmans, S. Levine, and P. Abbeel, “Multimodal masked autoencoders learn transferable representations,” *arXiv preprint arXiv:2205.14204*, 2022.

- [12] L. Zhou, H. Liu, J. Bae, J. He, D. Samaras, and P. Prasanna, “Self pre-training with masked autoencoders for medical image analysis,” in *ISBI*, 2023.
- [13] A. Dosovitskiy, L. Beyer, A. Kolesnikov, D. Weissenborn, X. Zhai, T. Unterthiner, M. Dehghani, M. Minderer, G. Heigold, S. Gelly, J. Uszkoreit, and N. Houlsby, “An image is worth 16x16 words: Transformers for image recognition at scale,” in *ICLR*, 2021.
- [14] H. Wagner, C. Chen, and E. Vućini, “Efficient computation of persistent homology for cubical data,” in *Topological Methods in Data Analysis and Visualization II: Theory, Algorithms, and Applications*, 2011, pp. 91–106.
- [15] S. Kaji, T. Sudo, and K. Ahara, “Cubical Ripser: Software for computing persistent homology of image and volume data,” *arXiv preprint arXiv:2005.12692*, 2020.
- [16] Y. Mileyko, S. Mukherjee, and J. Harer, “Probability measures on the space of persistence diagrams,” *Inverse Problems*, vol. 27, no. 12, pp. 124007, 2011.
- [17] B. Landman, Z. Xu, J. Igelsias, M. Styner, T. Langerak, and A. Klein, “MICCAI multi-atlas labeling beyond the cranial vault – workshop and challenge,” in *MICCAI Multi-Atlas Labeling Beyond Cranial Vault—Workshop Challenge*, 2015, p. 12.
- [18] M. Antonelli, A. Reinke, S. Bakas, K. Farahani, A. Kopp-Schneider, B. A. Landman, G. Litjens, B. Menze, O. Ronneberger, R. M. Summers, et al., “The medical segmentation decathlon,” *Nature Communications*, vol. 13, no. 1, pp. 4128, 2022.
- [19] A. Radford, L. Metz, and S. Chintala, “Unsupervised representation learning with deep convolutional generative adversarial networks,” *arXiv preprint arXiv:1511.06434*, 2015.
- [20] C. Ledig, L. Theis, F. Huszár, J. Caballero, A. Cunningham, A. Acosta, A. Aitken, A. Tejani, J. Totz, Z. Wang, et al., “Photo-realistic single image super-resolution using a generative adversarial network,” in *CVPR*, 2017, pp. 4681–4690.
- [21] D. Pathak, P. Krahenbuhl, J. Donahue, T. Darrell, and A. A. Efros, “Context encoders: Feature learning by inpainting,” in *CVPR*, 2016, pp. 2536–2544.
- [22] R. Zhang, P. Isola, and A. A. Efros, “Split-brain autoencoders: Unsupervised learning by cross-channel prediction,” in *CVPR*, 2017, pp. 1058–1067.
- [23] G. Larsson, M. Maire, and G. Shakhnarovich, “Colorization as a proxy task for visual understanding,” in *CVPR*, 2017, pp. 6874–6883.
- [24] M. Noroozi and P. Favaro, “Unsupervised learning of visual representations by solving Jigsaw puzzles,” in *ECCV*. Springer, 2016, pp. 69–84.
- [25] H. Lee, S. J. Hwang, and J. Shin, “Self-supervised label augmentation via input transformations,” in *ICML*. PMLR, 2020, pp. 5714–5724.
- [26] M. Caron, P. Bojanowski, A. Joulin, and M. Douze, “Deep clustering for unsupervised learning of visual features,” in *ECCV*, 2018, pp. 132–149.
- [27] T. Chen, S. Kornblith, M. Norouzi, and G. Hinton, “A simple framework for contrastive learning of visual representations,” in *ICML*. PMLR, 2020, pp. 1597–1607.
- [28] K. He, H. Fan, Y. Wu, S. Xie, and R. Girshick, “Momentum contrast for unsupervised visual representation learning,” in *CVPR*, 2020, pp. 9729–9738.
- [29] J.-B. Grill, F. Strub, F. Althé, C. Tallec, P. Richemond, E. Buchatskaya, C. Doersch, B. Avila Pires, Z. Guo, M. Gheshlaghi Azar, et al., “Bootstrap your own latent – a new approach to self-supervised learning,” *Advances in Neural Information Processing Systems*, vol. 33, pp. 21271–21284, 2020.
- [30] X. Chen and K. He, “Exploring simple siamese representation learning,” in *CVPR*, 2021, pp. 15750–15758.
- [31] P. Vincent, H. Larochelle, Y. Bengio, and P.-A. Manzagol, “Extracting and composing robust features with denoising autoencoders,” in *ICML*, 2008, pp. 1096–1103.
- [32] J. Devlin, M.-W. Chang, K. Lee, and K. Toutanova, “BERT: Pre-training of deep bidirectional Transformers for language understanding,” *arXiv preprint arXiv:1810.04805*, 2018.
- [33] J. An, Y. Bai, H. Chen, Z. Gao, and G. Litjens, “Masked autoencoders pre-training in multiple instance learning for whole slide image classification,” in *MIDL*, 2022.
- [34] S. T. Ly, B. Lin, H. Q. Vo, D. Maric, B. Roysam, and H. V. Nguyen, “Student collaboration improves self-supervised learning: Dual-loss adaptive masked autoencoder for brain cell image analysis,” *arXiv preprint arXiv:2205.05194*, 2022.
- [35] H. Quan, X. Li, W. Chen, M. Zou, R. Yang, T. Zheng, R. Qi, X. Gao, and X. Cui, “Global contrast masked autoencoders are powerful pathological representation learners,” *arXiv preprint arXiv:2205.09048*, 2022.
- [36] Y. Luo, Z. Chen, and X. Gao, “Self-distillation augmented masked autoencoders for histopathological image classification,” *arXiv preprint arXiv:2203.16983*, 2022.

- [37] J. Deng, W. Dong, R. Socher, L.-J. Li, K. Li, and L. Fei-Fei, “ImageNet: A large-scale hierarchical image database,” in *CVPR*, 2009, pp. 248–255.
- [38] A. Mosinska, P. Marquez-Neila, M. Kozifński, and P. Fua, “Beyond the pixel-wise loss for topology-aware delineation,” in *CVPR*, 2018, pp. 3136–3145.
- [39] S. Shit, J. C. Paetzold, A. Sekuboyina, I. Ezhov, A. Unger, A. Zhylyka, J. P. Pluim, U. Bauer, and B. H. Menze, “cIDice – a novel topology-preserving loss function for tubular structure segmentation,” in *CVPR*, 2021, pp. 16560–16569.
- [40] X. Hu, F. Li, D. Samaras, and C. Chen, “Topology-preserving deep image segmentation,” in *NeurIPS*, 2019.
- [41] J. R. Clough, N. Byrne, I. Oksuz, V. A. Zimmer, J. A. Schnabel, and A. P. King, “A topological loss function for deep-learning based image segmentation using persistent homology,” *IEEE Transactions on Pattern Analysis and Machine Intelligence*, vol. 44, no. 12, pp. 8766–8778, 2020.
- [42] X. Hu, Y. Wang, L. Fuxin, D. Samaras, and C. Chen, “Topology-aware segmentation using discrete Morse theory,” in *ICLR*, 2021.
- [43] C. Chen, X. Ni, Q. Bai, and Y. Wang, “A topological regularizer for classifiers via persistent homology,” in *ICAI*, 2019, pp. 2573–2582.
- [44] H. Wang, G. Huang, Z. Zhao, L. Cheng, A. Juncker-Jensen, M. L. Nagy, X. Lu, X. Zhang, and D. Z. Chen, “CCF-GNN: A unified model aggregating appearance, microenvironment, and topology for pathology image classification,” *IEEE Transactions on Medical Imaging*, 2023.
- [45] D. J. Waibel, S. Atwell, M. Meier, C. Marr, and B. Rieck, “Capturing shape information with multi-scale topological loss terms for 3D reconstruction,” in *MICCAI*, 2022, pp. 150–159.
- [46] P. Wu, C. Chen, Y. Wang, S. Zhang, C. Yuan, Z. Qian, D. Metaxas, and L. Axel, “Optimal topological cycles and their application in cardiac trabeculae restoration,” in *MICCAI*. Springer, 2017, pp. 80–92.
- [47] F. Wang, H. Liu, D. Samaras, and C. Chen, “TopoGAN: A topology-aware generative adversarial network,” in *ECCV*, 2020, pp. 118–136.
- [48] C. Chen and N. Quadrianto, “Clustering high dimensional categorical data via topographical features,” in *ICML*, 2016, pp. 2732–2740.
- [49] H. Wang, H. Zheng, and D. Z. Chen, “TANGO: A GO-term embedding based method for protein semantic similarity prediction,” *IEEE/ACM Transactions on Computational Biology and Bioinformatics*, vol. 20, no. 1, pp. 694–706, 2023.
- [50] O. Ronneberger, P. Fischer, and T. Brox, “U-Net: Convolutional networks for biomedical image segmentation,” in *MICCAI*, 2015, pp. 234–241.
- [51] O. Oktay, J. Schlemper, L. L. Folgoc, M. Lee, M. Heinrich, K. Misawa, K. Mori, S. McDonagh, N. Y. Hammerla, B. Kainz, et al., “Attention U-Net: Learning where to look for the pancreas,” *arXiv preprint arXiv:1804.03999*, 2018.
- [52] Z. Zhou, M. M. R. Siddiquee, N. Tajbakhsh, and J. Liang, “UNet++: A nested U-Net architecture for medical image segmentation,” in *DLMIA/ML-CDS*, 2018, pp. 3–11.
- [53] H. Huang, L. Lin, R. Tong, H. Hu, Q. Zhang, Y. Iwamoto, X. Han, Y.-W. Chen, and J. Wu, “UNet 3+: A full-scale connected unet for medical image segmentation,” in *ICASSP*, 2020, pp. 1055–1059.
- [54] D. Karimi, S. D. Vasylechko, and A. Gholipour, “Convolution-free medical image segmentation using Transformers,” in *MICCAI*. Springer, 2021, pp. 78–88.
- [55] H. Cao, Y. Wang, J. Chen, D. Jiang, X. Zhang, Q. Tian, and M. Wang, “Swin-UNet: UNet-like pure Transformer for medical image segmentation,” in *ECCV Workshops*, 2023, pp. 205–218.
- [56] J. Chen, Y. Lu, Q. Yu, X. Luo, E. Adeli, Y. Wang, L. Lu, A. L. Yuille, and Y. Zhou, “TransUNet: Transformers make strong encoders for medical image segmentation,” *arXiv preprint arXiv:2102.04306*, 2021.
- [57] A. Hatamizadeh, Y. Tang, V. Nath, D. Yang, A. Myronenko, B. Landman, H. R. Roth, and D. Xu, “UNETR: Transformers for 3D medical image segmentation,” in *WACV*, 2022, pp. 1748–1758.
- [58] X. Huang, Z. Deng, D. Li, and X. Yuan, “MISSFormer: An effective medical image segmentation Transformer,” *arXiv preprint arXiv:2109.07162*, 2021.
- [59] A. Hatamizadeh, V. Nath, Y. Tang, D. Yang, H. R. Roth, and D. Xu, “Swin UNETR: Swin Transformers for semantic segmentation of brain tumors in MRI images,” in *International MICCAI Brainlesion Workshop*, 2022, pp. 272–284.
- [60] W. Wang, C. Chen, M. Ding, H. Yu, S. Zha, and J. Li, “TransBTS: Multimodal brain tumor segmentation using Transformer,” in *MICCAI*, 2021, pp. 109–119.

- [61] Y. Xie, J. Zhang, C. Shen, and Y. Xia, “CoTr: Efficiently bridging CNN and Transformer for 3D medical image segmentation,” in *MICCAI*, 2021, pp. 171–180.
- [62] Y. Zhang, H. Liu, and Q. Hu, “TransFuse: Fusing Transformers and CNNs for medical image segmentation,” in *MICCAI*, 2021, pp. 14–24.
- [63] J. M. J. Valanarasu, P. Oza, I. Hacihaliloglu, and V. M. Patel, “Medical Transformer: Gated axial-attention for medical image segmentation,” in *MICCAI*, 2021, pp. 36–46.
- [64] P. Gu, Y. Zhang, C. Wang, and D. Z. Chen, “ConvFormer: Combining CNN and Transformer for medical image segmentation,” in *ISBI*, 2023.
- [65] H. Edelsbrunner, D. Letscher, and A. Zomorodian, “Topological persistence and simplification,” *Discrete & Computational Geometry*, vol. 28, pp. 511–533, 2002.
- [66] R. Flamary, N. Courty, A. Gramfort, M. Z. Alaya, A. Boisbunon, S. Chambon, L. Chapel, A. Corenflos, K. Fatras, N. Fournier, et al., “POT: Python optimal transport,” *The Journal of Machine Learning Research*, vol. 22, no. 1, pp. 3571–3578, 2021.
- [67] Y. Zhang, P. Gu, N. Sapkota, H. Zheng, P. Liang, and D. Z. Chen, “A point in the right direction: Vector prediction for spatially-aware self-supervised volumetric representation learning,” in *ISBI*, 2023.
- [68] O. Bernard, A. Lalande, C. Zotti, F. Cervenansky, X. Yang, P.-A. Heng, I. Cetin, K. Lekadir, O. Camara, M. A. G. Ballester, et al., “Deep learning techniques for automatic MRI cardiac multi-structures segmentation and diagnosis: Is the problem solved?,” *IEEE Transactions on Medical Imaging*, vol. 37, no. 11, pp. 2514–2525, 2018.
- [69] I. Loshchilov and F. Hutter, “Decoupled weight decay regularization,” in *ICLR*, 2019.
- [70] G. Xu, X. Wu, X. Zhang, and X. He, “LeVit-UNet: Make faster encoders with Transformer for medical image segmentation,” *arXiv preprint arXiv:2107.08623*, 2021.
- [71] S. Zheng, J. Lu, H. Zhao, X. Zhu, Z. Luo, Y. Wang, Y. Fu, J. Feng, T. Xiang, P. H. Torr, et al., “Rethinking semantic segmentation from a sequence-to-sequence perspective with Transformers,” in *CVPR*, 2021, pp. 6881–6890.